Journal of Materials Chemistry A

ROYAL SOCIETY OF CHEMISTRY

PAPER

View Article Online
View Journal | View Issue

Cite this: J. Mater. Chem. A, 2023, 11, 11903

Prediction of structurally stable two-dimensional $AuClO_2$ with high thermoelectric performance†

Puxin Cheng,[a] Geng Li,*[ab] Yinchang Zhao,[c] Xiangfei Meng,[b] Shuming Zeng*[d] and Jialiang Xu*[a]

Received 19th February 2023
Accepted 4th May 2023

DOI: 10.1039/d3ta01037f

rsc.li/materials-a

Numerous two-dimensional (2D) materials have been reported to exhibit remarkable thermoelectric (TE) performances owing to their quantum confinement effects. However, the identification of ideal TE materials with a low thermal conductivity (κ_L) and high Seebeck coefficient ($|S|$) remains a formidable challenge due to their high coupling and inherent conflict. In this work, a new monolayer semiconductor $AuClO_2$ with a balanced TE performance has been theoretically predicted by combining first-principles calculations with the Boltzmann transport equation. The results of phonon spectrum, molecular dynamic (MD) simulations, and mechanical property analyses suggest that $AuClO_2$ features thermodynamic and mechanical stability. Strikingly, $AuClO_2$ possesses an ultralow κ_L of 0.14 (0.45) W m^{-1} K^{-1} along the *a* (*b*)-axis at 300 K, thanks to its low phonon group velocity (v_{ph}) and short phonon lifetime (τ_{ph}). Furthermore, the flat valence bands of $AuClO_2$ promote a high $|S|$ under p-type doping, leading to large zT values in the range of 1.0–2.4 under different temperatures and even up to a maximum value of 2.35 at 900 K. This study offers a promising TE material for applications in fields such as thermal insulation and thermoelectric refrigeration, and provides theoretical guidelines for the design of high performance 2D TE materials.

Introduction

Two-dimensional (2D) materials have attracted wide interest from researchers since monolayer graphene was successfully exfoliated from bulk graphite in 2004.[1] As methods in both theory and experiment have advanced, plentiful 2D materials have come into sight,[2] including black phosphorus (BP),[3] transition metal dichalcogenides (TMDs),[4,5] group IVA–VIA compounds,[6] MXenes,[7] graphdiyne,[8] *etc.* These 2D materials feature unique electronic and mechanical properties thanks to their layered structural characteristics, making their broad application at the foreground in photoelectrochemical devices,[9–11] perovskite solar cells,[12] biomedicine,[13] catalysis and energy storage,[14] and nonlinear optics.[15–17] Some of these 2D materials, such as layered Bi_2Te_3, SnSe, and PbTe, also possess high thermoelectric (TE) performances and have been applied in fields such as power generation,[6,18–27] thermal insulation and low power thermoelectric refrigeration,[28,29] owing to their quantum confinement effects.

The conversion efficiency between the thermal and electrical energy of TE materials is evaluated by the dimensionless figure of merit, zT:

$$zT = \frac{S^2\sigma}{\kappa_L + \kappa_e} T \quad (1)$$

in which S, σ, κ_L, κ_e, and T denote the Seebeck coefficient, electronic conductivity, electronic thermal conductivity and temperature, respectively. However, it is difficult to identify an ideal material with high S and σ, along with low κ_L and κ_e, simultaneously. To search for TE materials with large zT, there are four strategies proposed in line with Slack's rule: (1) heavy atom mass, (2) weak interatomic bonding, (3) complex structure, and (4) strong anharmonic.[30–32] The strategy of using complicated low dimensional materials including 2D materials with heavy elements has been proven intuitive and effective. Yang *et al.* have theoretically studied the phonon thermal transport of a monolayer FeB_2 with a Dirac state in the Fermi level, which has a much lower κ_L of 51.9 W m^{-1} K^{-1} at 300 K than that of blue phosphorene and graphene due to the heavier Fe atoms.[33] Wang *et al.* have reported a metal-shrouded 2D material Tl_2O obtained from its corresponding layered bulk with a very low κ_L of 2.4 W m^{-1} K^{-1} at 300 K reduced by the heavy Tl atoms, along with a high zT of 3.55/4.20 under n/p-type dopants at 900 K.[34] Janus monolayer 2D materials (Sn/Pb)SSe

[a]School of Materials Science and Engineering, National Institute for Advanced Materials, Smart Sensing Interdisciplinary Science Center, Nankai University, Tongyan Road 38, Tianjin 300350, P. R. China. E-mail: jialiang.xu@nankai.edu.cn
[b]National Supercomputer Center in Tianjin, Tianjin 300457, P. R. China. E-mail: ligeng@nscc-tj.cn
[c]Department of Physics, Yantai University, Yantai 264005, P. R. China
[d]Department of Physics, Yangzhou University, Yangzhou 225009, P. R. China. E-mail: zengsm@yzu.edu.cn

† Electronic supplementary information (ESI) available. See DOI: https://doi.org/10.1039/d3ta01037f

and WS(Se/Te) with larger atomic mass in homogeneous structures have also been revealed to be ideal candidates for TE materials.[35,36] Very recently, Luo *et al.* have demonstrated experimentally that κ_L could be further diluted by introducing the heavy Pb atoms into the 2D $Bi_2Si_2Te_6$ semiconductor and a peak zT of 0.90 was captured at 723 K.[37]

Drawing inspiration from the on-going research on 2D TE materials with large atomic mass, we have identified a novel monolayer compound $AuClO_2$ filter from the 2DMatPedia database,[38] and theoretically studied its electronic and mechanical properties, thermodynamic stability, and TE properties. The results indicate that monolayer $AuClO_2$ is a thermodynamically and mechanically stable semiconductor with a direct band gap of 1.19 eV. This new 2D material features an ultralow lattice thermal conductivity κ_L of 0.14 (0.45) W m^{-1} K^{-1} at 300 K along the a (b)-axis due to the heavy Au atoms and weak interatomic bonding. Meanwhile, a large Seebeck coefficient $|S|$ could be obtained with optimal carrier concentration (n), and the largest value exceeds 0.80 mV K^{-1}. The coexistence of phonon and electronic transport performance gives rise to a high figure of merit zT under p-type doping within a range of 1.0–2.4 at medium–high temperature, which even could reach 2.35 (1.76) along the in-plane directions at 900 K, demonstrating the bright application prospect of the $AuClO_2$ 2D TE material.

Computational methodology

All the first-principles calculations are conducted in the Vienna *ab initio* simulation package (VASP), and the projector augmented-wave method (PAW) is adopted to simulate the interaction between ions and electrons.[39,40] The generalized gradient approximation of Perdew–Burke–Ernzerhof (GGA-PBE) has been selected to handle the exchange–correlation energy.[41] The cutoff energy of the plane-wave basis set is fixed at 520 eV. A Γ-centred 12 × 12 × 1 k-point grid is used to divide the Brillouin Zone (BZ) integration. The vacuum layer of 23 Å is set in the normal direction to prevent interaction in adjacent $AuClO_2$ monolayers. The energy convergence and the norms of the Hellmann–Feynman forces are set as 10^{-8} and 10^{-4}, respectively. In the molecular dynamics (MD) simulations, the temperature is set at 900 K for 5000 fs with a time step of 1 fs. On the basis of density functional perturbation theory (DFPT), Born effective charges and dielectric tensors are calculated to suit the nonanalytic part of the dynamic matrix.[42]

To investigate the lattice thermal transport properties, the HA interatomic force constants (IFCs) are acquired by the finite-displacement approach in a 3 × 2 × 1 supercell with a displacement of 0.01 Å, and the anharmonic IFCs from third to sixth order are captured by the compressive sensing (CS) lattice dynamics method in 60 stochastic structures, both of which are implemented in ALAMODE.[43–46] For the 2nd and 3rd IFC calculations, the interactions including the nearest neighbors with the cut-off radius of 17.70 Å are employed to promise the convergence, which are larger than the common values of 6.5 Å.[32,36,47–49] Phonon DOS is calculated using a 16 × 16 × 1 q-point mesh. According to the linearized phonon Boltzmann transport equations (BTE) of relaxation time approximation (RTA), the κ_L values have been achieved in a 16 × 16 × 1 q-point mesh and could be expressed as eqn (2):

$$\kappa_L^a(T) = \frac{1}{k_B T^2 \Omega N} \sum_\lambda f_0(f_0+1)(\hbar\omega_\lambda) v_\lambda^{a,\lambda} F_\lambda^a \quad (2)$$

where k_B and T are Boltzmann constants, and Ω, N, f_0, ω_λ, and $v_\lambda^{a,\lambda}$ stand for the volume of the unit cell, the number of k-points in BZ, the equilibrium Bose–Einstein distribution function, phonon frequency and phonon velocity of phonon mode λ along the a direction, respectively. The last term F_λ^a is further defined as a function of phonon relaxation time (τ_λ) and $v_\lambda^{a,\lambda}$, as shown in eqn (3):

$$F_\lambda^a = \tau_\lambda (v_\lambda^{a,\lambda} + \Delta_\lambda) \quad (3)$$

where Δ_λ denotes the correction term, and working in RTA can be reached when the value of Δ_λ is equal to 0.[50]

The electronic transport properties of $AuClO_2$ have also been calculated on the basis of electron BTE using the AMSET package.[51] The initial DFT calculations are performed under the PBE functional with a 14 × 14 × 1 k-point grid, which are the electronic structure, high frequency dielectric constants, and deformation potentials. The DFPT calculations have also been carried out to acquire the elastic constants, static dielectric constants, and effective polar phonon frequency. We have taken account of the fully anisotropic acoustic deformation potential (ADP) method to simulate the electron–acoustic phonon interaction, the polar electron–phonon (POP) method to deal with the electro-optical phonon interaction, and the ionized impurity scattering (IMP). The ADP method plays a significant part in anisotropic materials for the involvement of the perturbations from longitudinal (transverse) modes and anisotropy in the deformation response.[52] Thus, the rational carrier relaxation time τ can be written as eqn (4):

$$\frac{1}{\tau} = P^{ADP} + P^{POP} + P^{IMP} \quad (4)$$

The crystal structure is mechanically exfoliated from the bulk $AuClO_2$ with a space group of $C222_1$ (no. 20). All the crystal structures are visualized using the VESTA software package.[53]

Results and discussion

The top view and side view of the 2D orthogonal compound $AuClO_2$ are shown in Fig. 1(a). There are eight atoms in each unit cell. After complete geometric optimization, $AuClO_2$ adopts a space group of $P222_1$ (no. 17) and the optimized lattice constants are 3.89 Å and 7.20 Å along the a- and b-axes, respectively, contributing to the strong anisotropy. From the top view, each Au atom is coordinated with two O atoms and two Cl atoms, forming a plane quadrilateral, and the adjacent quadrilaterals joint together by sharing one of the Cl atoms. As can be seen from the side view, these quadrilaterals are arranged as zig-zag chains, with Au atoms sandwiched by O atoms and Cl atoms. The phonon dispersion spectrum suggests the

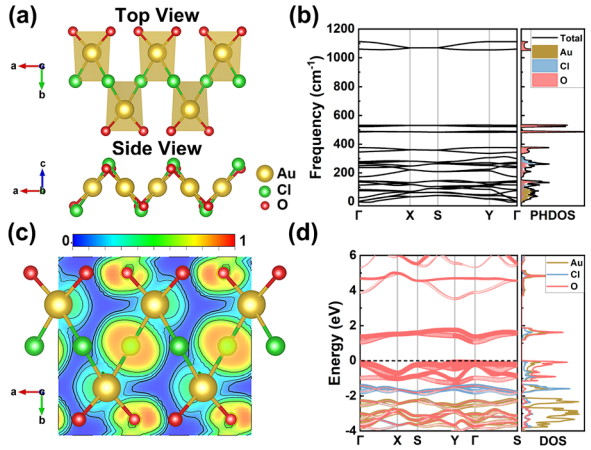

Fig. 1 (a) The optimized crystalline structure of $AuClO_2$ from top and side views. (b) The calculated phonon spectrum and relevant phonon density states (PDOS). (c) The 2D projected electron location function (ELF) of a 2 × 1 × 1 unit cell along the (001) plane. (d) The calculated electronic band structures and relevant density of states (DOS) under the GGA-PBE exchange–correction function.

thermodynamical stability for the absence of imaginary frequency, as shown in Fig. 1(b). It is evident from the relevant phonon density of states (PHDOS) that Au atoms with larger atomic mass contribute mainly to low-lying modes below 180 cm^{-1}, and high-frequency modes are constituted by Cl atoms and O atoms. A large interval (of about 520 cm^{-1}) has been found between the two highest-frequency modes and a smaller interval is located in the range of 380–500 cm^{-1}. The vibrations of O atoms have greatly contributed to these two pairs of discrete phonon bands.

To analyse the bonding properties of $AuClO_2$, the 2D ELF has been calculated and presented in Fig. 1(c). There are more localized electrons around Cl and O atoms, and less electron density around Au atoms, suggesting the weaker bonds of Au–Cl and Au–O, which are beneficial to obtain a low κ_L. We first investigate the basic electronic characteristics, as shown in Fig. 1(d) and S1.† The electronic band structure shows that $AuClO_2$ is a semiconductor with a direct band gap of about 1.19 eV. The conduction band minimum (CBM) and the valence band maximum (VBM) are both located at the Γ point, which are primarily constructed from the hybrid O-2p and Au-5d orbitals. It is noteworthy that the VBM exhibits relatively flat characteristics along Γ–S and Γ–Y directions, known as the "pudding-mold-type" band structure,[34,54,55] resulting in a rapid increase in DOS around Fermi energy. The electronic behaviour indicates a large band effective mass (m^*), which is favourable for the increase of $|S|$.[56,57]

MD simulations of monolayer $AuClO_2$ have been carried out to examine the structural stability, as shown in Fig. 2 and S3.† The small fluctuations in total energy and bond lengths indicate its thermodynamic stability until 800 K. When the temperature rises to 900 K, most chemical bonds can be well maintained, except for the severe vibrations of the Au–Cl_2 bond. Furthermore, the mechanical properties have been studied and the results as summarized in Table S1,† confirming the stability as

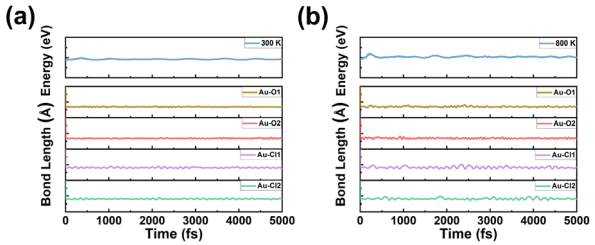

Fig. 2 The total energy and bond length fluctuation of $AuClO_2$ during MD simulations under (a) 300 K and (b) 800 K after 5000 fs, respectively.

the elastic constants satisfy the required criteria, which are $C_{11} > 0$, $C_{33} > 0$, and $C_{11} \times C_{22} > C_{12}^2$.[58–61]

The temperature-dependent κ_L of $AuClO_2$ has been investigated taking three-phonon scattering into consideration, as displayed in Fig. 3(a), which is vital in thermal transport performance. The distance between the topmost and bottommost Cl (h_{Cl-Cl}) is 2.78 Å, and the van der Waals radius of Cl (r_{Cl}) is 1.88 Å. Therefore, the effective thickness is treated as $h_{eff} = h_{Cl-Cl} + 2 \times r_{Cl}$ with a value of 6.54 Å,[62,63] as shown in Fig. S5.† The results reveal that the anisotropic thermal transport behaviour is related to the crystal structure, with ultralow κ_L values of 0.14 W m^{-1} K^{-1} and 0.45 W m^{-1} K^{-1} along the a- and b-axes at 300 K, respectively, which are much lower than those of typical TE materials such as layered Bi_2Te_3 ($\kappa_L \sim 1.2$ W m^{-1} K^{-1} @ 300 K),[21] PbTe ($\kappa_L \sim 2$ W m^{-1} K^{-1} @ 300 K),[24–26] and SnSe

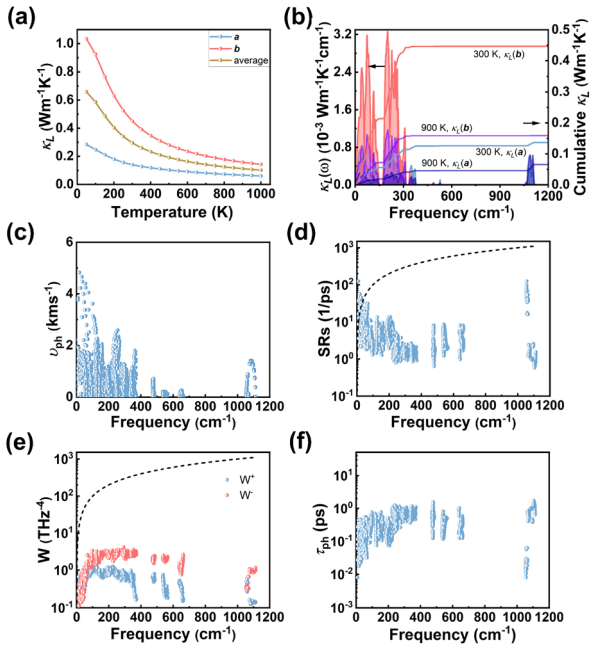

Fig. 3 (a) Temperature-dependent κ_L of $AuClO_2$ along the a- and b-axes. (b) Lattice thermal conductivity spectra $\kappa_L(\omega)$ and relevant cumulative κ_L along a- and b-axes at 300 K and 900 K. (c) Phonon group velocity (υ_{ph}), (d) scattering rates (SRs), (e) scattering phase spaces (W) for absorption and emission processes, and (f) phonon lifetime (τ_{ph}). The black dashed lines in (c) and (e) indicate the scattering rates equal to frequency, $1/\tau = \omega/2\pi$.

($\kappa_L \sim 0.5$ W m^{-1} K^{-1} @ 500 K).[6,23] The effect of different q-point meshes on κ_L values has been considered in Fig. S6.† It is found that the 16 × 16 × 1 q-point mesh is adequate to achieve relatively accurate results. In addition, the calculated lattice thermal conductivity curves along a- and b-axes have weak temperature dependence, $\kappa_L^a \propto T^{-0.48}$, and $\kappa_L^b \propto T^{-0.59}$. This unusual phenomenon is induced by the ignorance of thermal expansion and four-phonon scattering.[64] We have also adopted another method to calculate the κ_L values based on the ShengBTE mode,[65] which are relatively close to those under the ALAMODE code, as displayed in Fig. S7.†

To explore the origin of such an ultralow κ_L, we have looked into the key components in the light of eqn (2), including phonon frequency (ω), phonon group velocity (υ_{ph}), scattering rates (SRs), and phonon lifetime (τ_{ph}), as presented in Fig. 3(b)–(f). First, we compare the lattice thermal conductivity spectra $\kappa_L(\omega)$ and relevant cumulative κ_L along the a- and b-axes at 300 K with those at 900 K. The overall shapes of the $\kappa_L(\omega)$ spectra are similar, while the peak values move down as the temperature increases. Meanwhile, the vibration of phonon modes at around 1100 cm^{-1} contributed by O atoms enhances from 300 K to 900 K. It can be observed that the acoustic phonon modes and low-lying optical phonon modes are the main contributors to κ_L, which cause phonon–phonon scattering, thereby reducing κ_L. The cumulative κ_L reaches almost 80% when the phonon frequency reaches 300 cm^{-1}, which is in line with the distribution of phonon bands in Fig. 1(b). Low υ_{ph} is expected for the ultralow κ_L on account of the functional relation $\kappa_L \propto \upsilon_{ph}^2$, as well as small τ_{ph} ($\kappa_L \propto \tau_{ph}$). The maximum value of υ_{ph} is equal to 4.8 km s^{-1}, which is comparable to those of the classic 2D TE materials SnSe (~4.1 km s^{-1}), and PbTe (~4.0 km s^{-1}).[26,66] SRs, the inverse of τ_{ph}, are also considered in the calculations, taking the progress of three-phonon scattering and isotope scattering into account. Most of the data points are below the dashed line in Fig. 3(d), making the phonon quasiparticle picture effective. The small τ_{ph} is ascribed to a high possibility of scattering in scattering phase spaces (W). Fig. 3(e) unveils the available three-phonon scattering channels, which denotes that W^-, referred to as three-phonon emission progress, is dominant for $AuClO_2$. As a result, the combination of small υ_{ph} and τ_{ph} gives rise to low κ_L.

The promise of $AuClO_2$ for applications in TE devices is also determined by its electronic transport performances. Based on BTE, σ, $|S|$, and κ_e have been estimated by including the effects of ADP, IMP, and POP. The carrier concentration for n/p-type is in the range of 2.4 × 10^{11} to 2.4 × 10^{14} cm^{-2}, and the calculated results are shown in Fig. 4 and S8.† [32,66–70] It is inspiring to find that p-type-doped $AuClO_2$ has the potential to serve as a good 2D TE material. As a function of n, the σ of n-type $AuClO_2$ decreases evidently between 300 K and 900 K and σ along the b-axis is larger than that along the a-axis at the same temperature. As for hole doping, the values of σ in the in-plane directions are approaching under different temperature, except that along the a-axis at 300 K. In contrast, as n increases, $|S|$ exhibits downward trends at different temperatures. Compared to the n-type material, the p-type one exhibits a larger $|S|$ due to the flatter electronic bands around the VBM. The higher the temperature

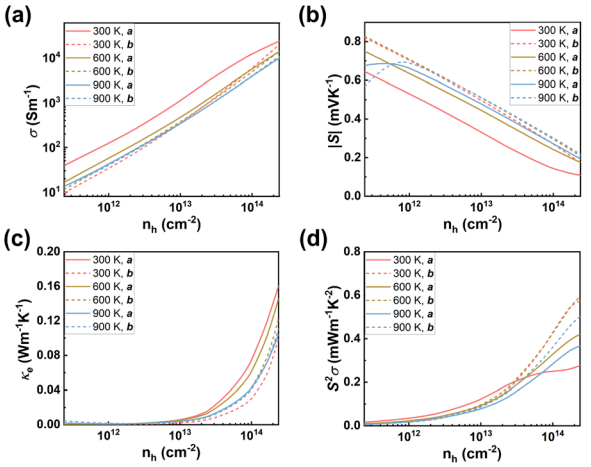

Fig. 4 The electronic transport parameters of p-type $AuClO_2$ at 300 K, 600 K and 900 K. (a) Electronic conductivity (σ), (b) Seebeck coefficient ($|S|$), (c) electronic thermal conductivity (κ_e), and (d) power factor ($S^2\sigma$) along a- and b-axes.

is, the larger the values of $|S|$ are, all exceeding 0.60 mV K^{-1} at the optimal n_h, which is comparable to those of SnSe (0.56 mV K^{-1} @ 900 K) and PbTe (0.60 mV K^{-1} @ 900 K).[26,66] The combination of σ and $|S|$ affects the power factor ($S^2\sigma$), leading to the maximum PF obtained as 0.59 mW m^{-1} K^{-2} along the b-axis at 600 K upon hole doping, which is slightly lower than those of the conventional TE materials such as $Bi_2Si_2Te_6$, SnSe and $SnSe_2$ under doping (0.6 to 1.2 mW m^{-1} K^{-2}).[6,37,70,71] Meanwhile, we have investigated κ_e, which is determined by the Wiedemann–Franz law ($\kappa_e = L\sigma T$, where L is the Lorentz number). Fig. 4(c) and S4c† demonstrate that κ_e is considerably influenced by temperature under high n. In brief, the optimal TE effect could be expected by selecting the appropriate concentration and temperature to reduce the total thermal conductivity.

The dimensionless TE figure of merit zT is widely used to evaluate TE properties as shown in Fig. 5, which combines phonon and electronic transport parameters. The zT value gets enlarged as temperature increases, and reaches the maximum at the optimal carrier concentration. It turns out that p-type $AuClO_2$ is provided with high zT values in the range of 1.0–2.4 at above 600 K, which could even reach 2.35 (1.76) @ 900 K along the a (b)-axis at $n_h \sim 10^{-14}$ cm^{-2}, higher than that of SnSe

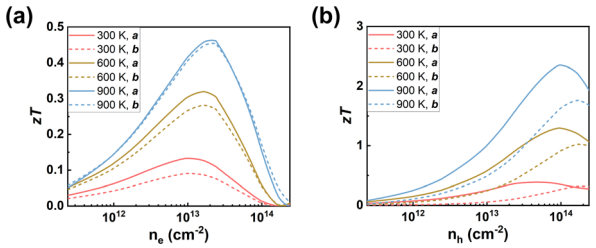

Fig. 5 The dimensionless TE figure of merit zT of (a) n-type $AuClO_2$, (b) p-type $AuClO_2$ along a- and b-axes at 300 K, 600 K and 900 K, respectively.

($zT \sim 1.34$ @ 773 K) and PbTe ($zT \sim 1.58$ @ 900 K),[26,66] making it a promising material for application in medium–high temperature TE devices such as thermal insulators and low power thermoelectric refrigerators.

Conclusions

In summary, we have carried out a thorough investigation on the electronic and mechanical properties, thermodynamic stability and TE properties of monolayer $AuClO_2$, using the combination of first-principles calculations and the BTE. Electronic structure studies indicate its semiconductor characteristics with a direct band gap of about 1.19 eV. The anisotropy in mechanical and TE properties is basically contributed by the unique atomic arrangements along the *a*- and *b*-axes. The calculation results confirm that the heavy Au atoms and strong localized electron density around Cl and O atoms play vital roles in achieving the ultralow κ_L with a value of 0.14 (0.45) W m^{-1} K^{-1} at 300 K along the *a* (*b*)-axis. Besides, due to the flat bands around the VBM, $AuClO_2$ is inclined to achieve a large $|S|$ under hole doping with the largest value exceeding 0.80 mV K^{-1}. Therefore, p-type $AuClO_2$ exhibits a high TE performance with zT values in the range of 1.0–2.4 under different temperatures, which supports its potential applications as a low dimensional TE material.

Conflicts of interest

There are no conflicts to declare.

Acknowledgements

Financial support from the National Natural Science Foundation of China (52172045 and 12204402) and the Fundamental Research Funds for the Central Universities is gratefully acknowledged. This work was also supported as part of a Multi-Scale and High-Efficiency Computing Platform for Advanced Functional Materials, a scientific research program funded by Haihe Laboratory in Tianjin (XCHK202110103). The authors acknowledge National Supercomputer Center in Tianjin, and the calculations were performed on Tianhe 3F.

References

1 K. S. Novoselov, A. K. Geim, S. V. Morozov, D. Jiang, Y. Zhang, S. V. Dubonos, I. V. Grigorieva and A. A. Firsov, *Science*, 2004, **306**, 666–669.
2 D. Li, Y. Gong, Y. Chen, J. Lin, Q. Khan, Y. Zhang, Y. Li, H. Zhang and H. Xie, *Nano-Micro Lett.*, 2020, **12**, 36.
3 L. Likai, Y. Yijun, Y. Guo Jun, Q. Ge, O. Xuedong, W. Hua, F. Donglai, C. Xian Hui and Z. Yuanbo, *Nat. Nanotechnol.*, 2014, **9**, 372–377.
4 Q. H. Wang, K. Kalantar-Zadeh, A. Kis, J. N. Coleman and M. S. Strano, *Nat. Nanotechnol.*, 2012, **7**, 699–712.
5 M. Zulfiqar, Y. Zhao, G. Li, Z. Li and J. Ni, *Sci. Rep.*, 2019, **9**, 4571.
6 C. Chang, M. Wu, D. He, Y. Pei, C.-F. Wu, X. Wu, H. Yu, F. Zhu, K. Wang, Y. Chen, L. Huang, J.-F. Li, J. He and L.-D. Zhao, *Science*, 2018, **360**, 778–783.
7 M. Naguib, V. N. Mochalin, M. W. Barsoum and Y. Gogotsi, *Adv. Mater.*, 2014, **26**, 992–1005.
8 C. Huang, Y. Li, N. Wang, Y. Xue, Z. Zuo, H. Liu and Y. Li, *Chem. Rev.*, 2018, **118**, 7744–7803.
9 Y. Zhou, H. Yin and S. Ai, *Coord. Chem. Rev.*, 2021, **447**, 214156.
10 H. Wei, R. Shi, L. Sun, H. Yu, J. Gong, C. Liu, Z. Xu, Y. Ni, J. Xu and W. Xu, *Nat. Commun.*, 2021, **12**, 1068.
11 Y. Zhang, P. Huang, J. Guo, R. Shi, W. Huang, Z. Shi, L. Wu, F. Zhang, L. Gao, C. Li, X. Zhang, J. Xu and H. Zhang, *Adv. Mater.*, 2020, **32**, 2001082.
12 S. Suragtkhuu, S. Sunderiya, P. Myagmarsereejid, S. Purevdorj, A. S. R. Bati, B. Bold, Y. L. Zhong, S. Davaasambuu and M. Batmunkh, *Adv. Energy Mater.*, 2023, 2204074.
13 J. A. Carrasco, P. Congost-Escoin, M. Assebban and G. Abellan, *Chem. Soc. Rev.*, 2023, **52**, 1288–1330.
14 Y. Zhu, L. Peng, Z. Fang, C. Yan, X. Zhang and G. Yu, *Adv. Mater.*, 2018, **30**, 1706347.
15 Y. Zhang, R. Shi, A. Kuklin, C. Ma, H. Chen, Y. Shu, X. Liu, Y. Fu, B. O. Al-Amoudi, S. Wageh, A. A. Al-Ghamdi, H. Ågren, J. Xu and H. Zhang, *Nano Today*, 2022, **47**, 101653.
16 Y. Dong, S. Semin, Y. Feng, J. Xu and T. Rasing, *Chin. Chem. Lett.*, 2021, **32**, 525–528.
17 L. Wu, Y. Dong, J. Zhao, D. Ma, W. Huang, Y. Zhang, Y. Wang, X. Jiang, Y. Xiang, J. Li, Y. Feng, J. Xu and H. Zhang, *Adv. Mater.*, 2019, **31**, 1807981.
18 Q. Zhong, Z. Dai, J. Liu, Y. Zhao and S. Meng, *Mater. Today Commun.*, 2020, **25**, 101441.
19 M. S. Dresselhaus, G. Dresselhaus, X. Sun, Z. Zhang, S. B. Cronin and T. Koga, *Phys. Solid State*, 1999, **41**, 679–682.
20 Y. Jia, Q. Jiang, H. Sun, P. Liu, D. Hu, Y. Pei, W. Liu, X. Crispin, S. Fabiano, Y. Ma and Y. Cao, *Adv. Mater.*, 2021, **33**, e2102990.
21 H. J. Goldsmid, *Materials*, 2014, **7**, 2577–2592.
22 F. Jia, Y. Y. Liu, Y. F. Zhang, X. Shu, L. Chen and L. M. Wu, *J. Am. Chem. Soc.*, 2020, **142**, 12536–12543.
23 Y. Xiao, C. Chang, Y. Pei, D. Wu, K. Peng, X. Zhou, S. Gong, J. He, Y. Zhang, Z. Zeng and L.-D. Zhao, *Phys. Rev. B*, 2016, **94**, 125203.
24 Z. Tian, J. Garg, K. Esfarjani, T. Shiga, J. Shiomi and G. Chen, *Phys. Rev. B: Condens. Matter Mater. Phys.*, 2012, **85**, 184303.
25 Y. Lu, T. Sun and D.-B. Zhang, *Phys. Rev. B*, 2018, **97**, 174304.
26 D. Zhang, S. Hu, Y. Sun, X. Liu, H. Wang, H. Wang, Y. Chen and Y. Ni, *ES Energy Environ.*, 2020, **10**, 59–65.
27 M. Samanta, T. Ghosh, S. Chandra and K. Biswas, *J. Mater. Chem. A*, 2020, **8**, 12226–12261.
28 Y. Amouyal, *Materials*, 2017, **10**, 386.
29 R. A. Kishore, A. Nozariasbmarz, B. Poudel, M. Sanghadasa and S. Priya, *Nat. Commun.*, 2019, **10**, 1765.
30 G. A. Slack, *J. Phys. Chem. Solids*, 1973, **34**, 321.
31 J. Sun, M. Hu, C. Zhang, L. Bai, C. Zhang and Q. Wang, *Adv. Funct. Mater.*, 2022, **32**, 2209000.

32 S. Tang, M. Wu, S. Bai, D. Luo, J. Zhang, D. Wan and X. Li, *J. Mater. Chem. C*, 2022, **10**, 16116–16125.
33 X. Yang, Z. Dai, Y. Zhao and S. Meng, *Comput. Mater. Sci.*, 2018, **147**, 132–136.
34 C. Wang, S. Wei and G. Gao, *ACS Appl. Nano Mater.*, 2019, **2**, 4061–4066.
35 A. Patel, D. Singh, Y. Sonvane, P. B. Thakor and R. Ahuja, *ACS Appl. Mater. Interfaces*, 2020, **12**, 46212–46219.
36 S. Bai, S. Tang, M. Wu, D. Luo, J. Zhang, D. Wan and S. Yang, *Appl. Surf. Sci.*, 2022, **599**, 153962.
37 Y. Luo, Z. Ma, S. Hao, S. Cai, Z. Z. Luo, C. Wolverton, V. P. Dravid, J. Yang, Q. Yan and M. G. Kanatzidis, *J. Am. Chem. Soc.*, 2022, **144**, 1445–1454.
38 J. Zhou, L. Shen, M. D. Costa, K. A. Persson, S. P. Ong, P. Huck, Y. Lu, X. Ma, Y. Chen, H. Tang and Y. P. Feng, *Sci. Data*, 2019, **6**, 86.
39 G. F. u. Kresse and J., *Phys. Rev. B: Condens. Matter Mater. Phys.*, 1996, **54**, 11169–11186.
40 G. J. Kresse and D., *Phys. Rev. B: Condens. Matter Mater. Phys.*, 1999, **59**, 1758–1775.
41 J. P. Perdew, K. Burke and M. Ernzerhof, *Phys. Rev. Lett.*, 1996, **77**, 3865–3868.
42 S. Baroni, S. de Gironcoli, A. Dal Corso and P. Giannozzi, *Rev. Mod. Phys.*, 2001, **73**, 515.
43 K. Esfarjani and H. T. Stokes, *Phys. Rev. B: Condens. Matter Mater. Phys.*, 2008, **77**, 144112.
44 F. Zhou, B. Sadigh, D. Åberg, Y. Xia and V. Ozoliņš, *Phys. Rev. B*, 2019, **100**, 184309.
45 T. Tadano and S. Tsuneyuki, *Phys. Rev. B: Condens. Matter Mater. Phys.*, 2015, **92**, 054301.
46 T. Tadano, Y. Gohda and S. Tsuneyuki, *J. Phys.: Condens. Matter*, 2014, **26**, 225402.
47 L. Zhu, G. Zhang and B. Li, *Phys. Rev. B: Condens. Matter Mater. Phys.*, 2014, **90**, 214302.
48 G. Qin, X. Zhang, S.-Y. Yue, Z. Qin, H. Wang, Y. Han and M. Hu, *Phys. Rev. B*, 2016, **94**, 165445.
49 H. H. Huang, X. Fan, W. T. Zheng and D. J. Singh, *J. Mater. Chem. C*, 2021, **9**, 1804–1813.
50 Q. Zhong, Z. Dai, J. Liu, Y. Zhao and S. Meng, *Phys. E*, 2020, **115**, 113683.
51 A. M. Ganose, J. Park, A. Faghaninia, R. Woods-Robinson, K. A. Persson and A. Jain, *Nat. Commun.*, 2021, **12**, 2222.
52 T. Yue, Y. Sun, Y. Zhao, S. Meng and Z. Dai, *Phys. Rev. B*, 2022, **105**, 054305.
53 K. Momma and F. Izumi, *J. Appl. Crystallogr.*, 2008, **41**, 653–658.
54 D. T. Do and S. D. Mahanti, *AIP Conf. Proc.*, 2017, **2005**, 020005.
55 K. Kuroki and R. Arita, *J. Phys. Soc. Jpn.*, 2007, **76**, 083707.
56 G. J. Snyder and E. S. Toberer, *Nat. Mater.*, 2008, **7**, 105–114.
57 Y. Zhao, C. Lian, S. Zeng, Z. Dai, S. Meng and J. Ni, *Phys. Rev. B*, 2020, **102**, 094314.
58 R. Hill, *Proc. Phys. Soc. A*, 1952, **65**, 349–354.
59 A. Reuss, *Z. Angew. Math. Mech.*, 1929, **9**, 49–58.
60 O. L. Anderson, *J. Phys. Chem. Solids*, 1963, **24**, 909–917.
61 M. Maździarz, *2D Mater.*, 2019, **6**, 048001.
62 Q. Y. Xie, J. J. Ma, Q. Y. Liu, P. F. Liu, P. Zhang, K. W. Zhang and B. T. Wang, *Phys. Chem. Chem. Phys.*, 2022, **24**, 7303–7310.
63 Z. Tong, T. Dumitrica and T. Frauenheim, *Nano Lett.*, 2021, **21**, 4351–4356.
64 Y. Xia, *Appl. Phys. Lett.*, 2018, **113**, 073901.
65 W. Li, J. Carrete, N. A. Katcho and N. Mingo, *Comput. Phys. Commun.*, 2014, **185**, 1747–1758.
66 L.-D. Zhao, G. Tan, S. Hao, J. He, Y. Pei, H. Chi, H. Wang, S. Gong, H. Xu, V. P. Dravid, C. Uher, G. J. Snyder, C. Wolverton and M. G. Kanatzidis, *Science*, 2015, **351**, 141–144.
67 B. Marfoua and J. Hong, *J. Mater. Chem. C*, 2021, **9**, 10497–10504.
68 W. L. Tao, Y. Q. Zhao, Z. Y. Zeng, X. R. Chen and H. Y. Geng, *ACS Appl. Mater. Interfaces*, 2021, **13**, 8700–8709.
69 N. Gaonkar and R. Vaidya, *Phys. Status Solidi RRL*, 2022, **16**, 2200129.
70 Y. Luo, Y. Zheng, Z. Luo, S. Hao, C. Du, Q. Liang, Z. Li, K. A. Khor, K. Hippalgaonkar, J. Xu, Q. Yan, C. Wolverton and M. G. Kanatzidis, *Adv. Energy Mater.*, 2018, **8**, 1702167.
71 T. Deng, Z. Gao, P. Qiu, T. R. Wei, J. Xiao, G. Wang, L. Chen and X. Shi, *Adv. Sci.*, 2022, **9**, 2203436.